Università degli Studi di Padova

DIPARTIMENTO DI FISICA E ASTRONOMIA "G. GALILEI"
Corso di Laurea in Fisica

Tesi di Laurea

Study of material activation in nanosatellites for gamma-ray astrophysics

Candidato:
Sara Andreetta
Matricola 1097274

Relatore:
Prof. Riccardo Rando

Anno Accademico 2016/2017

Ai miei genitori, a mio fratello Gianluca, a Alberto

Index

Chapter 1

Introduction

The framework of this thesis is gamma-rays astrophysics. In particular, we focus on instruments operating in the Compton regime between about 100 keV to approximately 10 MeV. Material activation has an impact on the spectroscopy capabilities of such instruments, since it causes an internal and structured background in the energy range of interest.

In the recent past, some missions in gamma rays studied the energetic interval from about 40 MeV and several TeV, x-ray and hard x-ray missions explored energies inferior to some hundreds of keV . Today a new generation of missions, like e-ASTROGAM [4] and AMEGO [15], is proposed for the intermediate energies, where coverage is relatively poor. The scientific return from observations in this energy range is really vast (see e.g. [4]) and can provide unique informations, useful to understand the physical processes powering several cosmic accelerators.

The predecessor COMPTEL (see section 2.2.1), showed that the internal background due to material activation, producing events in the energy range of the signals, is a serious problem. In this work, we choose to analyze the problem with a quick and simple design: a nanosatellite silicon-based Compton telescope.

The particles, which interact with the satellite, can be subdivided in primary and secondary. In this work, the consequences of the *primary protons* are studied.

Chapter 2

Analysis of the problem

2.1 Space background

The Compton region is also the region of nuclear decay lines, which let us investigate the chemical content of several astrophysical objects. Because of absorption from the Earth's atmosphere, it is necessary to place instruments in orbit. Even in Low Earth Orbit (with an altitude <2000 km a.s.l.), there is a rich radioactive environment with energetic particles; neutrons and the fraction of ions that can surmount the Coulomb barrier create nuclear reactions and produce radioisotopes, which then decay. In this way an instrumental gamma-ray background is created, composed by a continuum with several characteristic lines.

2.2 The nanosatellite

We will investigate the case of a Compton nanosatellite. We choose to use a nanosatellite because of several reasons. First of all, simulations are easier because of the small volume; in addition, even a nanosatellite mission can have a scientific return: see for more details [5] and [1]. Our main concern here is that emitted photons may ultimately be accepted as valid events, limiting the performance of the instrument.

In our work the satellite's geometry is very simplified: there is a calorimeter block made by CsI, then there are 30 layers of Silicon, then 4 bars of Aluminum, which constitute the support structure, and all these pieces are enclosed by the anticoincidence, made with a plastic scintillator (see figure 2.1). For more details see section 3.1 and for the motivation of this design, see [5] and [1].

The nanosatellite is supposed to be orbiting the Earth at altitudes of 550 km with an inclination of 5°; we assume launch in 2020, at solar minimum.

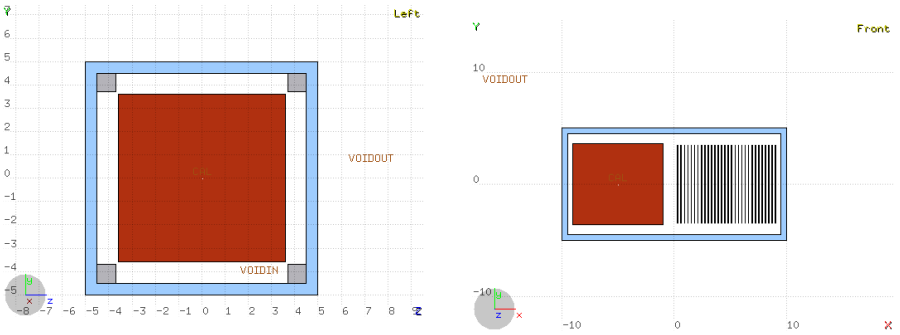

(a) Top view (b) Side view

Figure 2.1: Geometry of the nanosatellite

2.2.1 The predecessor: COMPTEL

In 1991 the Compton Gamma-Ray Observatory was launched with its four gamma-ray instruments; one of these was COMPTEL [16], a ton-scale payload, which explored the 1 - 30 MeV energy range. It had two detector layers D1 and D2, the first made of organic scintillator (composed mostly of hydrogen and carbon), the second one consisting of NaI(Tl) crystals in an Aluminum housing.

COMPTEL orbited the Earth at altitudes of 350-500 km with an inclination of 28.5°, from 1991 to 2000. It encountered a complex and variable radiation environment, whose main constituents were primary particles coming from outside the Solar System and secondary particles created locally. One byproduct was production of a background of gamma-ray photons due to material activation. The spectrum was analyzed in [11]; eight different isotopes have been identified: ^{2}D, ^{22}Na, ^{24}Na, ^{28}Al, ^{40}K, ^{52}Mn, ^{57}Ni and ^{208}Tl.

2.3 Primary and secondary particles

The particles involved can be subdivided in primary and secondary: the primary particles originate from interstellar space, they are mostly protons and it is not totally clear the way how they are produced. If they have enough rigidity, they can reach the payload; lower rigidity particles and secondaries, caused by interaction of primaries with the atmosphere, can be trapped and confined by magnetic field ("radioactive belts").

2.3.1 Secondary particles

In 1958 it was discovered that Earth is surrounded by regions rich in energetic ions and electrons. They have different origin and they behave dy-

namically: in fact the electric and magnetic field accelerate, confine and transport these particles.

To understanding particle trapping in the Earth's magnetic field, it is possible to derive the drift and mirror equations starting from Lorentz equations. An energetic particle introduced into the geomagnetic field gyrates around the field lines; the parallel motion will take the particle towards the poles of the Earth, where the field gradient causes the particles to be reflected.

Even though at first approximation the geomagnetic field can be seen as a dipole field, there are some asymmetries in the interior current system that introduce higher-order terms which imply the distortion of the isointensity lines; much of this distortion is caused by the non alignment of the magnetic axis with the spin axis of the Earth (11.3°) and the center of the magnetic dipole is not at the center of Earth (about 3000 km). There is a large region of reduced field on the east coast of South America, which is known as the South Atlantic Anomaly, SAA; this area is important, because in LEO most of the energetic particles are located here. The secondary particles have approximately energies $<100MeV$.

2.3.2 Primary particles

Primary particles are charged particles that have been accelerated by various astrophysical sources somewhere in the Universe. With manned missions and an increasing number of satellites orbiting the Earth, the characterization of the radiation dose received in different moments of the solar cycle is really important.

Many models (see e.g. [6]) have been proposed to describe the propagation of cosmic-rays within the heliosphere and into the Earth's magnetic field: with force-field approximation and assuming a spherical symmetry, radial solar wind, an isotropic diffusion coefficient and no particle drift, the differential flux of cosmic rays $\frac{dJ(T)}{dT}$ is related to the LIS $\frac{dJ_{LIS}}{dT}$ via:

$$\frac{dJ(T)}{dT} = \frac{T(T+2M)}{(T+\Phi)(T+\Phi+2M)} \frac{dJ(T+\Phi)_{LIS}}{dT} \tag{2.1}$$

In equation 2.1 T is the kinetic energy of a nucleus of charge Z and mass M and $\Phi = Ze\phi(t)$, where $\phi(t)$ is known as the solar modulation parameter, varying from about 400 MV at solar minimum to more than 1000 MV at solar maximum.

In 2006, the PAMELA experiment [3] was launched in LEO and provided direct measurements of the proton flux and its variations up to 50 GeV. In [3] the proton fluxes measured by PAMELA are fitted by a new LIS model based on Voyager 1 and AMS-02 proton data. In [3], they proposed a modified version of the force-field approximation with an energy-dependent ϕ to better describe PAMELA data.

The last obstacle for the galactic cosmic rays on their way to the atmosphere is the geomagnetic field. The cosmic ray flux on top of the atmosphere is therefore non isotropic and depends on the detector position; Stoermer [9] had solved analytically the equation of motion of a dipole field and the complete formula for the Stoermer rigidity cutoff is:

$$R_S(r, \lambda_B, \theta, \phi_B) = \frac{M}{2r^2} \left\{ \frac{\cos^4 \lambda_B}{[1 + (1 - \cos^3 \lambda_B \sin\theta \sin\phi_B)^{1/2}]^2} \right\} \tag{2.2}$$

where θ is the particle zenith angle and ϕ_B is the azimuthal angle measured clockwise from the direction of the magnetic south, λ_B is the magnetic latitude and M is the magnetic dipole moment of the Earth.

2.4 Nuclear decays

Radioactive decay is the process in which an unstable nucleus spontaneously emitts ionizing particles and radiation to reach a more energetically favorable (stable) configuration. An atom of one type, called the parent nuclide, transforms into an atom of a different type, named the daughter nuclide. The radioactive decay is a statistical process and the time at which the decay happens is random. However, looking at a large ensemble of nuclei, it is possible to predict at each instant the average number of decays and of parent and daughter nuclides.

2.4.1 Some basic concepts

If the number of radioactive nuclei is N, the number of decaying atoms per unit time is $\frac{dN}{dt}$. The decay rate is proportional to the number of nuclei themselves, as show in the formula 2.3:

$$\frac{dN}{dt} = -\lambda N(t) \tag{2.3}$$

The constant λ is called the decay constant and equation 2.3 can be rewritten as:

$$\lambda = -\frac{\frac{dN}{dt}}{N} \tag{2.4}$$

This leads to to the exponential law of radioactive decay:

$$N(t) = N(0)e^{-\lambda t} \tag{2.5}$$

It is then possible to define the mean lifetime τ as:

$$\tau = \frac{1}{\lambda} \tag{2.6}$$

and the half-time as:

$$t_{1/2} = \frac{ln(2)}{\lambda} \tag{2.7}$$

At the end, activity is defined as:

$$A(t) = \lambda N(t) \tag{2.8}$$

Some nuclei only decay via a single process, but sometimes they can decay in several different radioactive processes that compete each other. If this happens, the formula that describes the decay constant is:

$$\frac{1}{\lambda} = \frac{1}{\lambda_1} + \frac{1}{\lambda_2} + \dots \tag{2.9}$$

Moreover if there is a production process with constant rate a, then:

$$\frac{dN}{dt} = a - \lambda N(t) \tag{2.10}$$

from which:

$$N(t) = \frac{a}{b}(1 - e^{-\lambda t}) \tag{2.11}$$

So $N(t)$ saturates exponentially to an equilibrium value N_∞ with a time constant which is again λ.

2.4.2 Hadronic interactions: nuclear fragmentation

Nuclei are complicated systems of neutrons and protons, that are held together by several forces. The nuclear binding energy E_b of a nucleus of mass A, consisting of N neutrons and Z protons, is given by the difference between the masses of the constituent nucleons and the nucleus itself. From energy conservation, one can also calculate what is the energy required to separate a fragment F containing N_F neutrons and Z_F protons from the nucleus: this separation energy is equal to the difference in the binding energy of the original nucleus and the two residual nuclei in the final state

Generally one could distinguish two types of nucleons in a nuclear collision: the participants have direct collisions with nucleons from the other colliding nucleus, the spectators are the rest of the nucleons, which do not participate directly at it. These last are however excited by the collision, gaining energy from collisions with some of the participant nucleons.

Since nuclear fragmentation is a very complex process, which cannot be described only in analytic terms, it is necessary to rely on measurements of the partial and total cross-sections.

Chapter 3

Method

3.1 Environment conditions

For the radiation source of our system, we had to define the radiation spectrum. The average interstellar spectrum is available in many parametrization, e.g. in [3] based on Voyager 1, AMS-02 and PAMELA. As we wrote in the previous chapter, the effect of the Sun is to add a modulation, most simply described by a single parameter, the solar modulation potential ϕ (in force-field approximation). For our work the solar modulation can be neglected respect to the geomagnetic one. To simplify the problem, we assume a cutoff at R=11 GV for the whole orbit, neglecting variation with geomagnetic coordinates along the orbit and with the pitch angle.

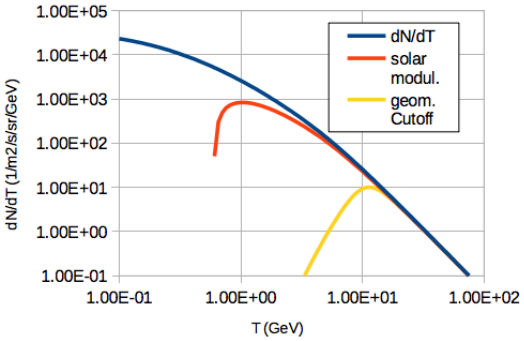

Figure 3.1: Proton spectrum: LIS and after cutoffs

The proton spectrum used in this work is shown in figure 3.1; the total flux is generated on a sphere with a radius of 20 cm surrounding the payload, isotropically towards the inside. Even though in reality the total flux is not homogeneous, we assumed it for our simulations because of simplicity.

Integrating the spectrum in figure 3.2, we obtain the beam intensity for our irradiation, which is 444 $particles/second$.

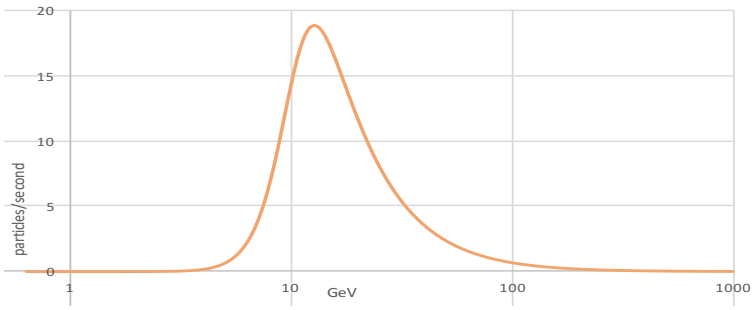

Figure 3.2: Total flux generated

Our nanosatellite is composed by:

- A Plastic scintillator anticoincidence, with a mass density of 1.032 g/cm^3 (its mass composition is C at 91.5 % and H at 8.5%): it is a box with an external area of $(20 \times 10 \times 10) cm^3$ and thickness of 1 cm
- 30 layers of Silicon, which constitute the tracker: each of them has a volume of $(0.05 \times 7 \times 7) cm^3$, separated by 0.3 cm
- 4 bars of Aluminum, which constitute the support structure: each of them has a volume of $(19 \times 0.8 \times 0.8) cm^3$ and they are located in the four corners
- A calorimeter of Cesium Iodide: it has a volume of $(8 \times 7.2 \times 7.2) cm^3$

The total mass of the nanosatellite is 3 kg. Shielding is negligible: even in Cesium Iodide the penetrating range for energy of 10 GeV is 1639 cm.

In the next tabel 3.1 it's possible to see for each part of the instrument its material and its total volume; see figure 2.1 for more details.

Part	Structure	Material	Volume cm^3
Structure	4 bars	Aluminum	48.64
Tracker	30 layers	Silicon	73.5
Calorimeter	block	Cesium Iodide	414.72
Anticoincidence	box	Plastic Scintillator	848

Table 3.1: Material

3.2 Monte Carlo simulations

For the Monte Carlo simulations of the interactions of particles and the decay of unstable isotopes, we used FLUKA [13].

3.2.1 What is FLUKA

FLUKA is fully integrated particle physics Monte Carlo simulation package. It has many applications in high-energy experimental physics and engineering, detector and telescope design, cosmic ray studies and many other. *flair* [14] is an advanced user friendly interface for FLUKA to facilitate the editing of FLUKA input files, execution of the code and visualization of the output files.

FLUKA operation is based on an input file, in which one sets several parameters: the main ones are the geometry of the system, its materials and the spectrum of the incoming particles. Moreover it is possible to choose the required outputs, such as the histograms of the residual nuclei presented in the next chapter. After the particles and interactions are simulated, nuclear decays are evaluated analytically.

3.2.2 The INPUT configuration

The input file of FLUKA is made by several blocks and in each of these the different parameters are set. In this work we used the following:

- flux:
  - we set the value of the flux according to the values in [3], considering the geomagnetic cutoff fixed at 11 GV, as explained in the previous section
  - the flux is generated inward of a sphere with 20 cm radius and it is isotropic
  - the number of particles/second is 444 particles/second
  - nuclear decays are evaluated after an irradiation time of one month
  - 10^8 number of primary histories to be simulated in the run, in order to have a good statistic
- geometry:
  - we set in the input file the same geometry as shown in figure 2.1
  - we assigned the materials to each part: Aluminum for the structure elements, Silicon for the tracker, Cesium Iodide for the calorimeter and Plastic scintillator for the anticoincidence
- output:
  - we want the histograms of the residual isotopes
  - we want histograms of the currents from a single subsystem of the nanosatellite into the payload (the other parts are sealed during the decay phase to avoid contaminations)

3.3 Procedure and results' analysis

We chose to make a simulation with an irradiation time interval long one month, in order to have a time interval comparable to a real observation time (typically about $10^6 s$). We focused our analysis of the produced unstable nuclides on those that produce gamma rays in our interval, between 200 keV to few MeV and on those that have a branching ratio greater than 1%.

Nuclear data are taken from an online database [12], this includes their products, their decay modes and branching ratios. Then, matching the decay's rates and the products' rates, we calculated for the six most intense gamma rays emitters the production rate, expressed in $gamma/second$.

We also checked if the half-times of the main residual radioisotopes found in the materials corresponded to the half-times scored in the database [12]: in this way we were able to check that there was not concurrence between different decay channels.

We have also taken the current that enter in the payload of the nanosatellite and we have analyzed them: for this reason the other subsystems were made hermetic, in order to separate the different contributes.

Chapter 4

Results

For each material we will report the residual nuclei at t=1 *month* (for Aluminum you'll find an example of saturation plot); there will be a table with all the isotopes, their activity, their half-time, their decay mode and the energy of produced gamma rays. After this, you will find a table of the gamma rays produced by activation and their rate, we do not indicate the different branching ratios (they are presented in the online database [12]). We also show current plots, scoring gamma rays leaving the various subsystems toward the inside of the payload, at t=$10^7 s$. Such plots are useful to compare the gamma fluxes with the expected amount from the decay of radionuclides, but show additional features. In particular we observe the 511 keV line from positron decay. How many of these internal gamma rays would cause a background event must be studied with a dedicated simulation of the instrument, including trigger and reconstruction.

4.1 Support structure (Al)

The activity of residual nuclei in Aluminum is shown in 4.1.

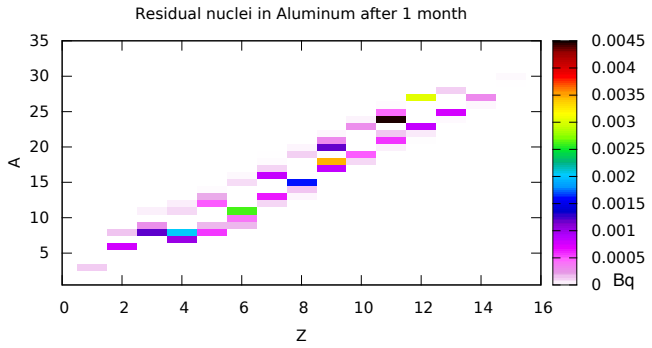

Figure 4.1: Activity of residual nuclei in Aluminum

We choose to report in detail the six most intense gamma-ray lines. In table 4.1 we show the corresponding isotopes, with activity and half-time.

Isotope	Activity $[Bq]$	$T_{1/2}$ and error	Decay	γ produced $[keV]$
${}^{20}_{9}F$	$(1.17 \pm 0.05) \cdot 10^{-3}$	11.00 (2) s	β^-	1633.602
${}^{24}_{11}Na$	$(4.46 \pm 0.03) \cdot 10^{-3}$	14.9590 (12) h	β^-	1368.633; 2754.028
${}^{27}_{12}Mg$	$(3.03 \pm 0.05) \cdot 10^{-3}$	9.458 (12) m	β^-	843.740; 1014.420
${}^{24m}_{11}Na$	$(2.22 \pm 0.02) \cdot 10^{-3}$	20.20 (7) ms	IT	472.202

Table 4.1: Residual isotopes in Aluminum

In table 4.2 we show the line centroid, the gamma emission rate (function of the isotope activity and of the branching ratio). "Saturation" indicates whether the corresponding decay has reached equilibrium in one month.

Energy $[keV]$	Rate $[\gamma/s]$	Decay mode	Saturation	Provenience
472.202	$(2.22 \pm 0.02) \cdot 10^{-3}$	IT	yes	${}^{24m}_{11}Na$
843.740	$(2.17 \pm 0.03) \cdot 10^{-3}$	β^-	yes	${}^{27}_{12}Mg$
1014.420	$(8.47 \pm 0.13) \cdot 10^{-4}$	β^-	yes	${}^{27}_{12}Mg$
1368.633	$(4.46 \pm 0.03) \cdot 10^{-3}$	β^-	yes	${}^{24}_{11}Na$
1633.602	$(1.17 \pm 0.05) \cdot 10^{-3}$	β^-	yes	${}^{20}_{9}F$
2754.028	$(4.45 \pm 0.03) \cdot 10^{-3}$	β^-	yes	${}^{24}_{11}Na$

Table 4.2: Main gamma rays produced in Aluminum

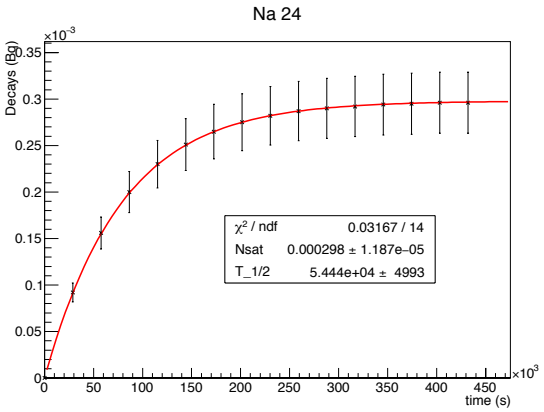

Figure 4.2: Saturation in ${}^{24}_{11}Na$

In Aluminum we found a great compatibility between the expected half-time and the simulated half-time for all the analyzed isotopes; this is proof that other decay chains do not contribute. As an example, we show the measurement for ${}^{24}_{11}Na$ in figure 4.2. The parameters of the exponential fit are the value of the activity at saturation and the half-time of the isotope; the expected value of the half-time is $5.39 \cdot 10^4\ s$.

In figure 4.3 we show the current of gamma rays entering the payload from Aluminum. For reference, the rate at 511 keV is $0.0137 \pm 0.0002\ ph/s$ (continuum-subtracted).

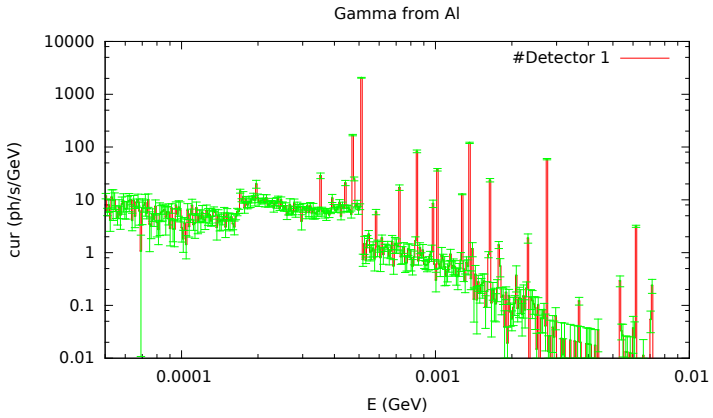

Figure 4.3: Differential plot of the gamma-ray current exiting the subsystem toward the inside of the payload in Aluminum

4.2 Tracker (Si)

The activity of residual nuclei in Silicon is shown in 4.4.

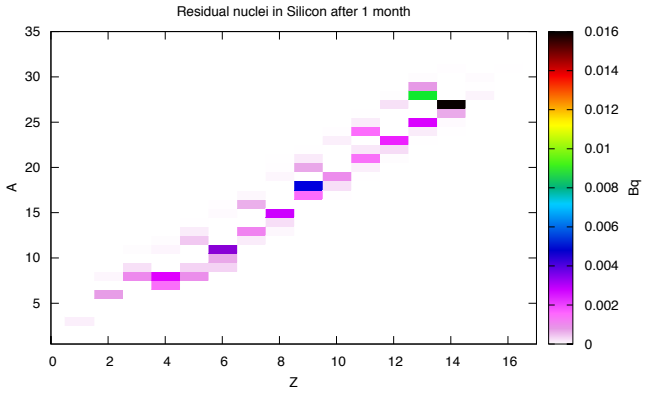

Figure 4.4: Activity of residual nuclei in Silicon

We choose to report in detail the six most intense gamma-ray lines.

In table 4.3 we show the corresponding isotopes, with activity and half-time.

Isotope	Activity $[Bq]$	$T_{1/2}$ and error	Decay	γ produced $[keV]$
$^{20}_{9}F$	$(6.93 \pm 0.19) \cdot 10^{-4}$	11.00 (2) s	β^-	1633.602
$^{24}_{11}Na$	$(1.51 \pm 0.02) \cdot 10^{-3}$	14.9590 (12) h	β^-	1368.633; 2754.028
$^{28}_{13}Al$	$(8.90 \pm 0.03) \cdot 10^{-3}$	2.214 (12) m	β^-	1778.969
$^{29}_{13}Al$	$(8.04 \pm 0.23) \cdot 10^{-4}$	6.56 (6) m	β^-	1273.367
$^{24m}_{11}Na$	$(7.47 \pm 0.08) \cdot 10^{-4}$	20.20 (7) ms	IT	472.202

Table 4.3: Residual isotopes in Silicon

In table 4.4 we show the line centroid, the gamma emission rate (function of the isotope activity and of the branching ratio).

"Saturation" indicates whether the corresponding decay has reached equilibrium in one month.

Energy $[keV]$	Rate $[\gamma/s]$	Decay mode	Saturation	Provenience
472.202	$(7.47 \pm 0.08) \cdot 10^{-4}$	IT	yes	$^{24m}_{11}Na$
1273.367	$(7.28 \pm 0.21) \cdot 10^{-4}$	β^-	yes	$^{29}_{13}Al$
1368.633	$(1.51 \pm 0.02) \cdot 10^{-3}$	β^-	yes	$^{24}_{11}Na$
1633.602	$(6.93 \pm 0.19) \cdot 10^{-4}$	β^-	yes	$^{20}_{9}F$
1778.969	$(8.90 \pm 0.09) \cdot 10^{-3}$	β^-	yes	$^{28}_{13}Al$
2754.028	$(4.45 \pm 0.03) \cdot 10^{-3}$	β^-	yes	$^{24}_{11}Na$

Table 4.4: Main gamma rays produced in Silicon

In Silicon we found a great compatibility between the expected half-time and the simulated half-time for all the analyzed isotopes; this is proof that other decay chains do not contribute.

In figure 4.5 we show the current of gamma rays entering the payload from Silicon.

For reference, the rate for 511 keV gamma rays is 0.0215 ± 0.0003 ph/s (continuum-subtracted).

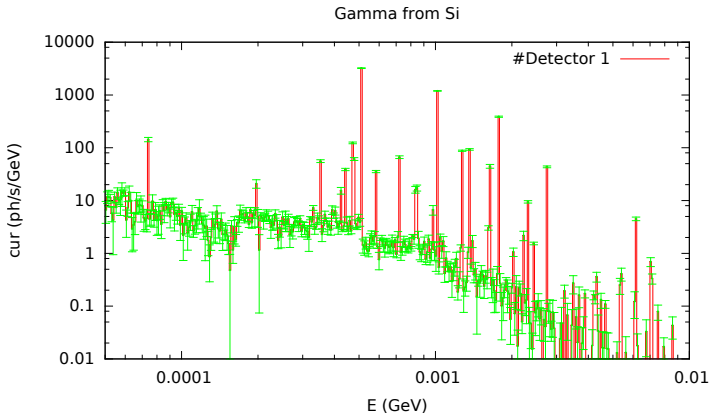

Figure 4.5: Differential plot of the gamma-ray current exiting the subsystem toward the inside of the payload in Silicon

4.3 Calorimeter (CsI)

The activity of residual nuclei in Cesium Iodide is shown in 4.6.

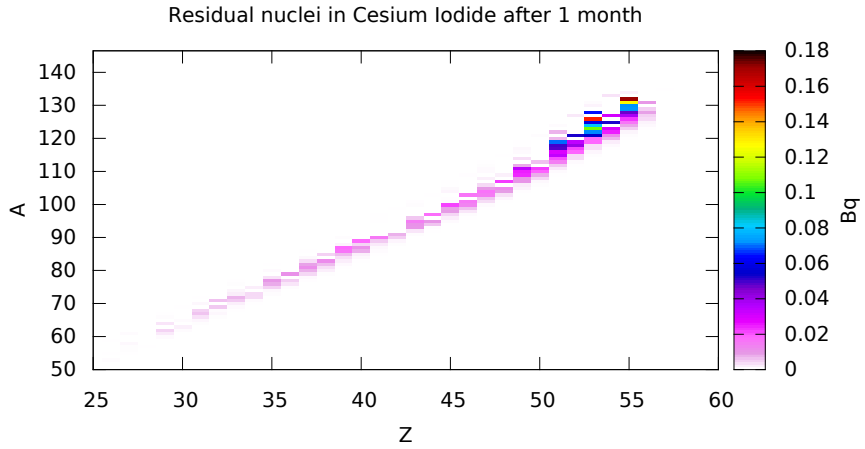

Figure 4.6: Activity of residual nuclei in Cesium Iodide

We choose to report in detail the six most intense gamma-ray lines. In table 4.5 we show the corresponding isotopes, with activity and half-time.

In table 4.6 we show the line centroid, the gamma emission rate (function of the isotope activity and of the branching ratio). "Saturation" indicates whether the corresponding decay has reached equilibrium in one month.

For reference, the rate for 511 keV gamma rays is 0.377 ± 0.001 ph/s (continuum-subtracted).

Isotope	Activity $[Bq]$	$T_{1/2}$ and error	Decay	γ produced $[keV]$
$^{121}_{53}I$	$(5.44 \pm 0.02) \cdot 10^{-2}$	2.12 (1) h	$e^+\beta^+$	212.189
$^{123}_{53}I$	$(1.072 \pm 0.004) \cdot 10^{-1}$	13.27 (8) h	$e^+\beta^+$	158.970
$^{124}_{53}I$	$(7.99 \pm 0.02) \cdot 10^{-2}$	4.1760 (3) d	$e^+\beta^+$	602.729
$^{126}_{53}I$	$(1.510 \pm 0.005) \cdot 10^{-1}$	13.11 (5) d	β^-	388.633
$^{126}_{53}I$	$(1.510 \pm 0.005) \cdot 10^{-1}$	13.11 (5) d	$e^+\beta^+$	666.331
$^{132}_{55}Cs$	$(1.706 \pm 0.004) \cdot 10^{-1}$	6.479 (7)d	$e^+\beta^+$	667.718

Table 4.5: Residual isotopes in Cesium Iodide

Energy $[keV]$	Rate $[\gamma/s]$	Decay mode	Saturation	Provenience
158.970	$(8.90 \pm 0.03) \cdot 10^{-2}$	$e^+\beta^+$	yes	$^{123}_{53}I$
212.189	$(4.57 \pm 0.04) \cdot 10^{-2}$	$e^+\beta^+$	yes	$^{121}_{53}I$
388.633	$(5.15 \pm 0.02) \cdot 10^{-2}$	β^-	no	$^{126}_{53}I$
602.729	$(5.04 \pm 0.01) \cdot 10^{-2}$	$e^+\beta^+$	no	$^{124}_{53}I$
666.331	$(5.00 \pm 0.02) \cdot 10^{-2}$	$e^+\beta^+$	no	$^{126}_{53}I$
667.718	$(1.672 \pm 0.004) \cdot 10^{-1}$	$e^+\beta^+$	yes	$^{132}_{55}Cs$

Table 4.6: Main gamma rays produced in Cesium Iodide

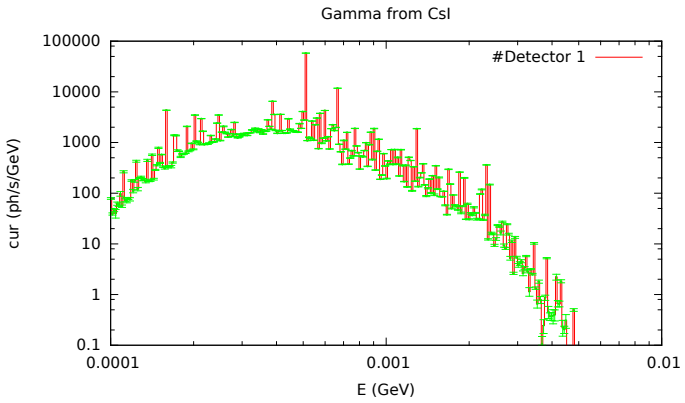

Figure 4.7: Differential plot of the gamma-ray current exiting the subsystem toward the inside of the payload in Cesium Iodide

4.4 Anticoincidence detector (Plastic)

The activity of residual nuclei in the Plastic scintillator is shown in 4.8.

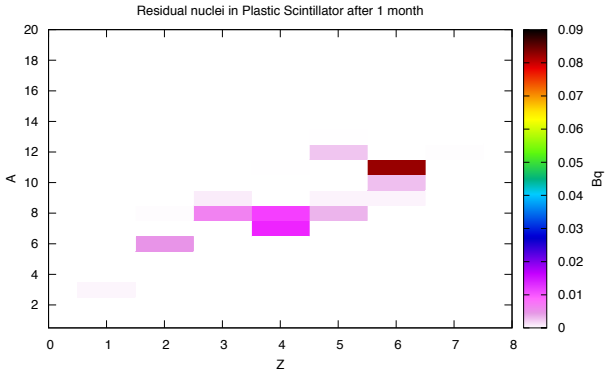

Figure 4.8: Activity of residual nuclei in Plastic Scintillator

We choose to report in detail the six most intense gamma-ray lines. In table 4.7 we show the corresponding isotopes, with activity and half-time.

Isotope	Activity $[Bq]$	$T_{1/2}$ and error	Decay	γ produced $[keV]$
${}^{8}_{2}He$	$(1.20 \pm 0.04) \cdot 10^{-4}$	119.0 (15) ms	β^-	980.700
${}^{7}_{4}Be$	$(1.196 \pm 0.005) \cdot 10^{-2}$	53.12 (7) d	e	477.595
${}^{11}_{4}Be$	$(4.74 \pm 0.83) \cdot 10^{-5}$	13.81 (8) s	β^-	2124.473; 4443.930
${}^{10}_{6}C$	$(2.82 \pm 0.05) \cdot 10^{-3}$	19.255 (53) s	$e^+\beta^+$	718.300; 1021.700

Table 4.7: Residual isotopes in Plastic Scintillator

In table 4.8 we show the line centroid, the gamma emission rate (function of the isotope activity and of the branching ratio). "Saturation" indicates whether the corresponding decay has reached equilibrium in one month.

Energy $[keV]$	Rate $[\gamma/s]$	Decay mode	Saturation	Provenience
477.595	$(1.258 \pm 0.005) \cdot 10^{-3}$	e	no	${}^{7}_{4}Be$
718.300	$(2.78 \pm 0.05) \cdot 10^{-3}$	$e^+\beta^+$	yes	${}^{10}_{6}C$
980.700	$(1.01 \pm 0.04) \cdot 10^{-4}$	β^-	yes	${}^{8}_{2}He$
1021.700	$(4.13 \pm 0.08) \cdot 10^{-5}$	$e^+\beta^+$	yes	${}^{10}_{6}C$
2124.473	$(4.74 \pm 0.83) \cdot 10^{-5}$	β^-	yes	${}^{11}_{4}Be$
4443.930	$(4.74 \pm 0.83) \cdot 10^{-5}$	β^-	yes	${}^{11}_{4}Be$

Table 4.8: Main gamma rays produced in Plastic Scintillator

In the anticoincidence the differential plot of the gamma-ray current

exiting the subsystem toward the inside of the payload is not reported, because we should remove all that causes a veto.

Chapter 5

Conclusion

5.1 Final summary

From the data shown in the previous chapter, one can see that there is a significant production rate of gamma rays. The main emitter, as expected, is the calorimeter with lines at 0.17 Hz.

To estimate the impact of this, we need a dedicate simulation to find out how many of these end up in a background event, after trigger, filter and reconstruction. For references, such a nanosatellite telescope has an overall event rate of the order of $\sim Hz$.

5.2 Future activities

There are a lot of possible future activities: in fact it will be interesting to study also the secondary particles, mentioned in the second chapter, and neutrons.

Results will have to be entered in the telescope simulation to quantify the background rates, as said above. Once everything is well understood, this procedure should be scaled to a full-scale insturment.

Bibliography

[1] F. Berlato. "Design and optimization around 1 MeV of a calorimeter for a CubeSat Mission". Master thesis. Università degli studi di Padova. (2016)

[2] P. Cappellaro. "Introduction to Applied Nuclear Physics". Lecture notes. Massachusetts Institute of Technology. (2012)

[3] C. Corti et al. "Solar Modulation of the Local Interstellar Spectrum with Voyager 1, AMS-02, PAMELA, and BESS". In: *The Astrophysical Journal, vol.829.* (2016)

[4] A. De Angelis et al. "The e-ASTROGAM mission - Exploring the extreme Universe with gamma rays in the MeV - GeV range". In: *Experimental Astrophysics.* (2017)

[5] G. Lucchetta. "Design and optimization around 1 MeV of a Tracker for a CubeSat Mission". Master thesis. Università degli studi di Padova. (2016)

[6] M. S. Potgieter. "Solar Modulation of Cosmic Rays". In: *Living Reviews in Solar Physics, vol. 10.* (2013)

[7] J. A. Ruiz et al. "Spallation products induced in CsI(Tl) by high-energy protons'. In: *The Astrophysical Journal Supplement Series, vol. 92, no. 2.* (1994)

[8] T. Stanev. "High Energy Cosmic Rays". Ed by *Springler.* (2004)

[9] C. Stoermer "Sur les trajectories des corpuscules electrises..." In: *Arch. Sci. Phys. Nat. Ser. 32.* (1911)

[10] M. Walt. "Introduction to Geomagnetically Trapped Radiation". Ed by *Cambridge University Press.* (1994)

[11] G. Weidenspointer. "The Origin of the Cosmic Gamma-Ray Background in the COMPTEL Energy Range". PhD thesis. Max Planck Institute for Extraterrestrial Physics. (1999)

[12] http://nucleardata.nuclear.lu.se/toi/nucSearch.asp

[13] http://www.fluka.org

[14] http://www.fluka.org/flair/

[15] https://asd.gsfc.nasa.gov/amego

[16] https://heasarc.gsfc.nasa.gov/docs/cgro/comptel/